Physics of the Earth and Planetary Interiors, 7 (1973) 251–265

GLOBAL ELECTROMAGNETIC INDUCTION IN THE MOON AND PLANETS

PALMER DYAL and CURTIS W. PARKIN
Space Science Division, NASA-Ames Research Center, Moffett Field, Calif. (U.S.A.)
Department of Physics, University of Santa Clara, Santa Clara, Calif. (U.S.A.)

Accepted for publication February 2, 1973

A summary of experiments and analyses concerning electromagnetic induction in the Moon and other extraterrestrial bodies is presented. Magnetic step-transient measurements made on the lunar dark side show the eddy current response to be the dominant induction mode of the Moon. Analysis of the poloidal field decay of the eddy currents has yielded a range of monotonic conductivity profiles for the lunar interior: the conductivity rises from $3 \cdot 10^{-4}$ mho/m at a depth of 170 km to 10^{-2} mho/m at 1000 km depth. The static magnetization field induction has been measured and the whole-Moon relative magnetic permeability has been calculated to be $\mu/\mu_0 = 1.01 \pm 0.06$. The remanent magnetic fields, measured at Apollo landing sites, range from 3 to 327 γ. Simultaneous magnetometer and solar wind spectrometer measurements show that the 38-γ remanent field at the Apollo 12 site is compressed to 54 γ by a solar wind pressure increase of $7 \cdot 10^{-8}$ dyn/cm^2. The solar wind confines the induced lunar poloidal field; the field is compressed to the surface on the lunar subsolar side and extends out into a cylindrical cavity on the lunar antisolar side. This solar wind confinement is modeled in the laboratory by a magnetic dipole enclosed in a superconducting lead cylinder; results show that the induced poloidal field geometry is modified in a manner similar to that measured on the Moon. Induction concepts developed for the Moon are extended to estimate the electromagnetic response of other bodies in the solar system.

1. Introduction

In this paper we discuss experiments and analyses that have been published on induction in the Moon and then present a summary of concepts concerning electromagnetic induction properties of other extraterrestrial bodies. The classical theory of induction was developed by Faraday, Lenz, and Maxwell during the nineteenth century; the electromagnetic response of a sphere has been treated by Mie (1908), Debye (1909), Smythe (1950), and others. Induction in the Earth and other planetary-sized bodies has been studied by investigators including Chapman (1919), Lahiri and Price (1939), and Rikitake (1950, 1966). The application of induction methods to the case of the Earth with its oceans, ionosphere, and radial and azimuthal conductivity anomalies is difficult; however, it has proven to be one of the more productive techniques used experimentally to probe deep into the Earth. Results from Apollo magnetic observatories on the lunar surface show that electromagnetic induction methods developed to study the Earth are more suitable for the Moon due to a fortunate combination of lunar electrical properties and solar wind driving field properties. Similar methods may be applicable to other moonlike bodies (e.g., Mercury) and to planets where a landing will be difficult or impossible (e.g., the Jovian planets).

We consider first the theory of classical electromagnetic induction in a sphere and extend this treatment to the case of the Moon, where poloidal eddy-current response has been found experimentally to dominate other induction modes. Analysis of lunar poloidal induction yields lunar internal electrical conductivity and temperature profiles. Two poloidal-induction analytical techniques will be discussed: a transient-response method applied to time-series magnetometer data and a harmonic-analysis method applied to data numerically Fourier-transformed to the frequency domain, with emphasis on the former technique. Next we discuss complicating effects of the solar wind interaction with both induced poloidal fields and remanent steady fields. Then we present the static magnetization field induction mode, from which we calculate bulk magnetic permeability profiles. Finally, magnetic field measurements ob-

tained from the Moon and from fly-bys of Venus and Mars are examined to determine the feasibility of extending theoretical and experimental induction techniques to other bodies in the solar system.

2. Poloidal eddy-current induction in the Moon

In this section we discuss the electromagnetic response of a particular planetary-sized body, the Moon, to external electromagnetic driving fields (Fig. 1). We treat in detail only the special cases which have been found practical in analyzing properties of the Moon; since poloidal eddy-current response has been found to be the dominant induction mode in the Moon, this section will emphasize the poloidal mode and associated properties of the lunar interior. Two analytical techniques will be discussed in reference to lunar induction: a transient-response (time-dependent) technique and a Fourier-harmonic (frequency-dependent) analysis technique.

Various possible induced fields and plasma-interaction fields will exist in the vicinity of the global Moon's surface; for reference we write the sum of these fields as:

$$\boldsymbol{B}_A = \boldsymbol{B}_E + \boldsymbol{B}_S + \boldsymbol{B}_\mu + \boldsymbol{B}_P + \boldsymbol{B}_T + \boldsymbol{B}_F \qquad (1)$$

Here $\boldsymbol{B}_A$ is the total magnetic field on or near the lunar surface; $\boldsymbol{B}_E$ is the total external (e.g., solar or terrestrial) driving magnetic field; $\boldsymbol{B}_S$ is the steady remanent field (which may be of global or local extent); $\boldsymbol{B}_\mu$ is the magnetization field induced in permeable lunar material; $\boldsymbol{B}_P$ is the poloidal field caused by eddy currents induced in the lunar interior by changing external fields; $\boldsymbol{B}_T$ is the toroidal field corresponding to unipolar electrical currents driven through the Moon by the $-\boldsymbol{V}\times\boldsymbol{B}_E$ electric field ($\boldsymbol{V}$ is average velocity of solar wind plasma); and $\boldsymbol{B}_F$ is the total field associated with the hydromagnetic solar wind flow past the spherical body (e.g., plasma confinement or compression of the planetary permanent or induced fields, fields due to induced ionospheric currents, etc.).

In the case of the Moon, the external driving magnetic field ($\boldsymbol{B}_E$) can vary considerably with orbital position (Fig. 2); therefore, it is possible to study the various lunar properties separately through careful selection of data time periods. Average magnetic field conditions vary from relatively steady fields of magnitude $\sim 9\ \gamma$ ($1\ \gamma = 10^{-5}$ gauss) in the geomagnetic tail to mildly turbulent fields averaging $\sim 5\ \gamma$ in the free-streaming solar plasma region to turbulent fields averaging $\sim 8\ \gamma$ in the magnetosheath. The average solar wind velocity is ~ 400 km/sec in a direction approximately along the Sun–Earth line.

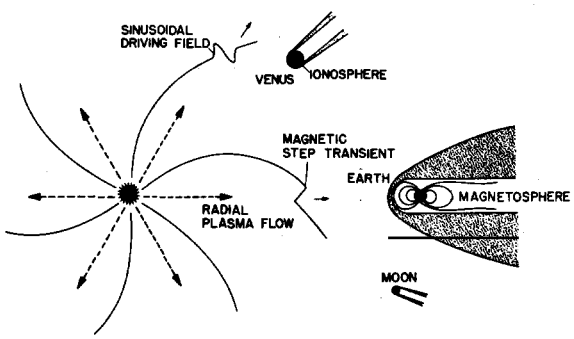

Fig. 1. Electromagnetic driving sources. This diagram schematically depicts external driving sources from the Sun and their interactions with planetary-sized bodies. A hot plasma, consisting primarily of protons and electrons, streams nearly radially outward from the Sun (at speeds averaging ~ 400 km/sec at Earth orbit), carrying a "frozen-in" magnetic field past the planets. Various types of magnetic discontinuities and wave phenomena act as time-varying driving functions to induce response fields in the planetary bodies and their ionospheres. Three different types of planetary-solar wind interactions are depicted here: one in which the planetary permanent magnetic field dominates in the interaction (in the case of the Earth), one where the planet's ionosphere dominates (as is probable in the case of Venus and Mars), and one where the solid planetary body itself dominates (the Moon).

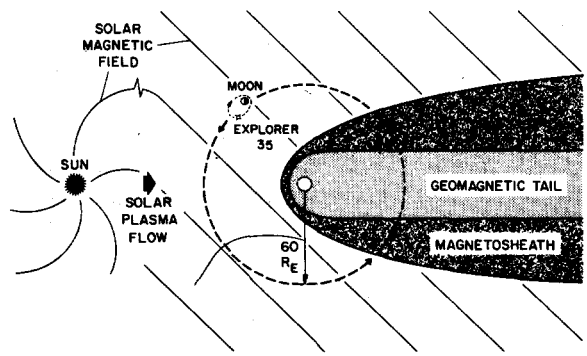

Fig. 2. Orbit of the Moon, projected onto the solar ecliptic plane. During a complete revolution around the Earth, the magnetometer passes through the Earth's bow shock, the magnetosheath, the geomagnetic tail, and the interplanetary region dominated by solar plasma fields. The Explorer 35 satellite orbit around the Moon is also shown.

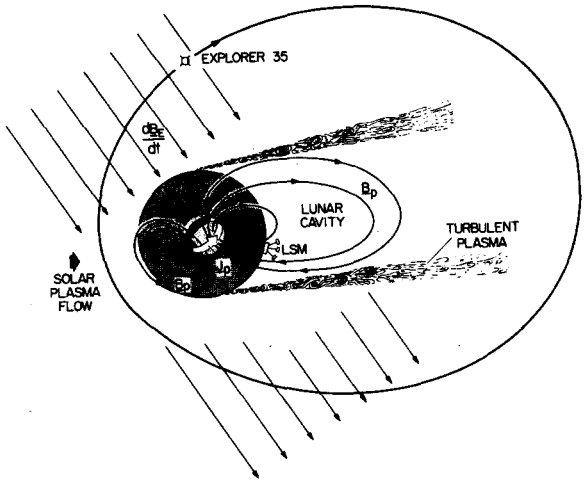

Fig. 3. Confinement of an induced global magnetic field by the solar wind. Conceptually depicted here is the case where a poloidal induced field $\boldsymbol{B}_P$ is confined by solar wind flow past the Moon. The induced field is compressed on the lunar sunlit side and confined in the vacuum cavity region on the antisolar dark side of the Moon. Also shown is the Explorer 35 magnetometer orbit projected onto the solar ecliptic plane. The Explorer 35 period of revolution is 11.5 h; its perilune and apolune are approximately 0.5 and 5 lunar radii, respectively.

The characteristics of each of the induction fields $\boldsymbol{B}_P$, $\boldsymbol{B}_T$ and $\boldsymbol{B}_\mu$ are dependent upon electromagnetic properties of the Moon's interior; therefore, these properties can be deduced from theoretical and experimental studies of the induction processes. The toroidal response field has been found to be generally much lower in magnitude than the poloidal field and perhaps not detectable by lunar magnetometers (Dyal and Parkin, 1972); therefore, the toroidal mode will not be discussed in detail in this paper. The magnetization field $\boldsymbol{B}_\mu$ is a function of global magnetic permeability and the iron content of the Moon; calculation of the lunar permeability will be included in a later section. The decay characteristics of the poloidal field $\boldsymbol{B}_P$, the dominant lunar induction mode (Fig.3), are a function of the global electrical conductivity distribution, which is in turn related to the global internal temperature distribution. This section includes calculation of lunar conductivity and temperature profiles using both time-series transient analysis and Fourier harmonic-analysis techniques.

2.1. Time-series transient analysis

2.1.1. Poloidal response of a homogeneous sphere in a vacuum

The global electromagnetic response of a planetary body is modeled by a sphere's response to a step-function transient magnetic field, which can be treated by extending the theory of Smythe (1950). The sphere is initially considered to be subject to the following conditions: (1) The sphere is in a vacuum, i.e., no plasma interactions (effects of the plasma are considered in section 3.1). (2) The sphere of radius R is homogeneous and has a constant permeability (μ), permittivity (ϵ) and conductivity (σ). (3) The dimensions of the external field transients are large compared to the sphere, such that the sphere responds as a whole to the transients. (4) Conduction currents dominate displacement currents within the sphere. (5) There is no net charge on the sphere. Then, for a coordinate system fixed in the sphere, Maxwell's equations and Ohm's law in the rationalized M.K.S. system are as follows:

$$\nabla \times \boldsymbol{E} = -\frac{\partial \boldsymbol{B}}{\partial t} \tag{2}$$

$$\nabla \times \boldsymbol{B} = \mu \boldsymbol{J} \tag{3}$$

$$\nabla \cdot \boldsymbol{E} = 0 \tag{4}$$

$$\nabla \cdot \boldsymbol{B} = 0 \tag{5}$$

$$\boldsymbol{J} = \sigma \boldsymbol{E} \tag{6}$$

where $\boldsymbol{E}$ and $\boldsymbol{B}$ are the electric field and the magnetic induction and $\boldsymbol{J}$ is the conduction current density.

Before we proceed to a more general transient analysis treatment, it is useful to consider the idealized case of a uniformly conducting sphere in a vacuum. This model is particularly applicable to fields measured on the antisolar side of the Moon, which is shielded from the solar plasma. Suppose that initially there is no magnetic field, but at $t = 0$ an external magnetic field $\Delta \boldsymbol{B}_E$ is switched on which is uniform far from the sphere. For the case of a homogeneous sphere in a vacuum Maxwell's equations can be solved by extending the theory of Smythe (1950); a detailed derivation is given by Dyal and Parkin (1971). Considering only the poloidal induction mode, eq. 1 becomes $\boldsymbol{B}_A = \boldsymbol{B}_E + \boldsymbol{B}_P$. The solution for the vector components

of the magnetic field at the surface of the sphere are listed below for the case of an external magnetic field step transient of magnitude $\Delta \boldsymbol{B}_E = \boldsymbol{B}_{Ef} - \boldsymbol{B}_{Eo}$ applied to the lunar sphere at time $t = 0$. $\boldsymbol{B}_{Eo}$ and $\boldsymbol{B}_{Ef}$ are initial and final external fields, respectively:

$$B_{Ax} = B_{Exf} - 3|\Delta B_{Ex}|F(t) \quad (7)$$

$$B_{Ay,z} = B_{Ey,zf} + \tfrac{3}{2}|\Delta B_{Ey,z}|F(t) \quad (8)$$

where:

$$F(t) = \frac{2}{\pi^2}\sum_{s=1}^{\infty}\frac{1}{s^2}\exp\left(\frac{-s^2\pi^2 t}{\mu\sigma R^2}\right) \quad (9)$$

σ is the electrical conductivity and μ is the magnetic permeability; and:

$$\Delta B_{Ei} = B_{Eif} - B_{Eio}, \quad i = x, y, z$$

The coordinate system used here has its origin on the surface of the sphere with the x-axis directed radially outward from the sphere's surface; the y- and z-axes are both tangential to the surface: y eastward and z northward. Qualitative representations of the solutions in eq.7 and 8 are illustrated in Fig.4A. It can be seen that if the "decay function" $F(t)$ can be determined empirically, then the electrical conductivity can be calculated from eq.9 for the homogeneous approximation.

Over one hundred step-transient events have been analyzed using Apollo 12 lunar surface magnetometer antisolar side data and simultaneous data from the lunar orbiting Explorer 35 magnetometer. These data show that the Moon's response is similar to the eddy-current response of a conducting sphere in a vacuum; measured surface magnetic field radial components have a damped response to solar wind field step transients, while components tangent to the lunar sphere have rapid response and overshoot initially, followed by decay to a steady-state value. An example of a step-transient event in Apollo 12 and Explorer 35 data is shown in Fig. 4B, and qualitative agreement between theory (eq. 7 and 8) and data is easily seen; the deviations of the data from homogeneous-sphere theory are considered in the following two sections.

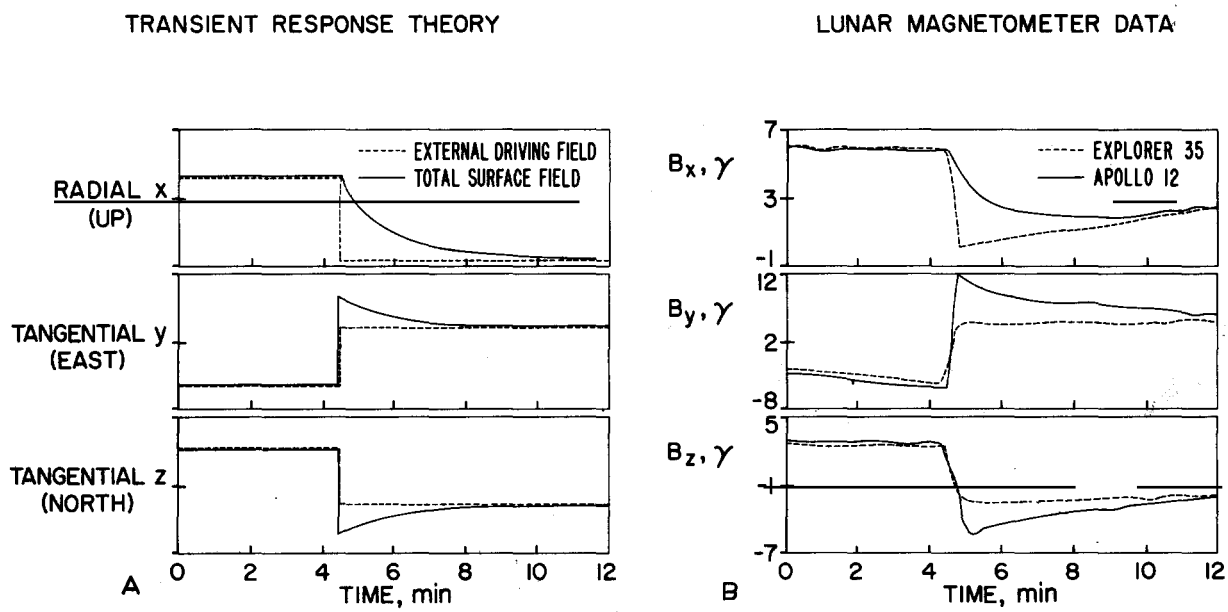

Fig. 4. Comparison of lunar magnetometer data to the theory for lunar poloidal response to a transient in the solar wind magnetic field. At left (A) are theoretical solutions of components of the surface field ($\boldsymbol{B}_A$) for a homogeneous sphere in a vacuum (see eq.7 and 8) which experiences step changes in all components of external driving field ($\boldsymbol{B}_E$). At right (B) are superimposed data plots of the external driving field $\boldsymbol{B}_E$ (measured by lunar orbiting Explorer 35) and total surface magnetic field $\boldsymbol{B}_A$ (measured by the Apollo 12 magnetometer while on the antisolar side of the Moon). In order to illustrate transients in all three components, these events were selected from different times during lunar night.

2.1.2. Poloidal response of a sphere of radially varying conductivity

To describe the response of the sphere to an arbitrary input (Dyal et al., 1972b), we define the magnetic vector potential A such that $\nabla \times A = B$ and $\nabla \cdot A = 0$. We seek the response to an input $\Delta B_E b(t)$, where $b(t) = 0$ for $t < 0$ and $b(t)$ approaches unity at $t \to \infty$. (Since the governing equations are linear, the response to a more general input is readily found by superposition.) The direction of ΔB_E is taken to be the axis of a spherical coordinate system (r, θ, φ). If the conductivity is spherically symmetric, the transient magnetic field response has no φ-component, and hence $A = A\hat{e}_\varphi$ and $\partial/\partial\varphi = 0$. Under these conditions (and neglecting displacement currents) the laws of Faraday, Ampère and Ohm combine to yield the diffusion equation for the magnetic potential (in M.K.S.-units):

$$\nabla^2 A(r, \theta; t) = \mu\sigma(r) \frac{\partial A}{\partial t}(r, \theta; t) \tag{10}$$

We assume $\mu = \mu_0$ everywhere (see section 4); then, for $t > 0$, the magnetic field must be continuous at the surface, so that A and $\partial A/\partial r$ must always be continuous at $r = R$, the radius of the sphere. We also have the boundary condition $A(0, t) = 0$ and the initial condition $A(r, \theta; 0) = 0$ inside the Moon. Outside of the Moon, where $\sigma = 0$:

$$A = \Delta B_E \left(\frac{r}{2}\right) b(t) \sin\theta + \frac{\Delta B_E}{r^2} f(t) \sin\theta \tag{11}$$

The first term on the right is a uniform magnetic field modulated by $b(t)$; the second term is the (as yet unknown) external transient response, which must vanish as $r \to \infty$ and $t \to \infty$. Note that at $r = R$, where R is normalized to unity:

$$A = \Delta B_E \sin\theta \left[\frac{b(t)}{2} + f(t)\right] \tag{12}$$

and:

$$\frac{\partial A}{\partial r} = \Delta B_E \sin\theta \left[\frac{b(t)}{2} - 2f(t)\right] \tag{13}$$

Therefore, at $r = R \equiv 1$:

$$\frac{\partial A}{\partial r} = -2A + \tfrac{3}{2}\left[\Delta B_E \sin\theta\, b(t)\right] \tag{14}$$

Since the magnetic field is continuous at $r = R$, this is a boundary condition for the interior problem. Letting $G(r, t) = A/\Delta B_E \sin\theta$ and $\bar{G}(r, s)$ be the Laplace transform of G, eq. 10 becomes:

$$\frac{1}{r}\left(\frac{\partial^2}{\partial r^2}(r\bar{G}) - \frac{2}{r}\bar{G}\right) = s\mu_0\sigma(r)\,\bar{G} \tag{15}$$

for the interior. The boundary conditions are:

$$\frac{\partial \bar{G}}{\partial r} = -2\bar{G} + \tfrac{3}{2}\bar{b}(s) \tag{16}$$

at $r = R$ and:

$$\bar{G} = 0 \tag{17}$$

at $r = 0$.

For a given $\sigma(r)$ and $b(t)$, this system is numerically integrated to obtain $\bar{G}(r, s)$ in the range $0 \leqslant r \leqslant R$. The function $\bar{G}(R, s)$ is then numerically inverse, Laplace-transformed to find the characteristic transient-response function $f(t)$ for the system. The resulting $f(t)$ is compared to the measurements and reiterated with a different function $\sigma(r)$ until the error between the calculated $f(t)$ and the measured $f(t)$ is minimized. The final $\sigma(r)$ is not unique; rather a family of $\sigma(r)$ is generated with the constraint that $f(t)$ match the experimental data.

2.1.3. Magnetic field measurements and calculation of electrical conductivity profile

Normalized lunar nighttime data from Apollo 12, giving the step-function response obtained from the radial surface field component (for eleven events) are shown in Fig. 5. Error bars are standard deviations of the measurements. All of these events ocurred when the magnetometer was more than 900 km inside the optical shadow, so that plasma effects are assumed to be minimal to first order (plasma effects are considered in section 3.1). Effects of the lunar cavity due to solar wind diamagnetism, described by Colburn et al. (1967) and Ness et al. (1967), are also neglected to a first approximation since the cavity field is a constant or very slowly varying function of time compared to the poloidal response time. Furthermore, recognizing the finite length of time required for a solar-wind step transient to pass the Moon, we have in our analysis chosen a ramp input function of 15-sec rise time, a time characterizing passage of a discontinuity past the Moon. (For a 400 km/sec solar wind, this time is 10–20 sec, depending on the thickness of the discontinuity and the inclination of its normal to the solar wind velocity.)

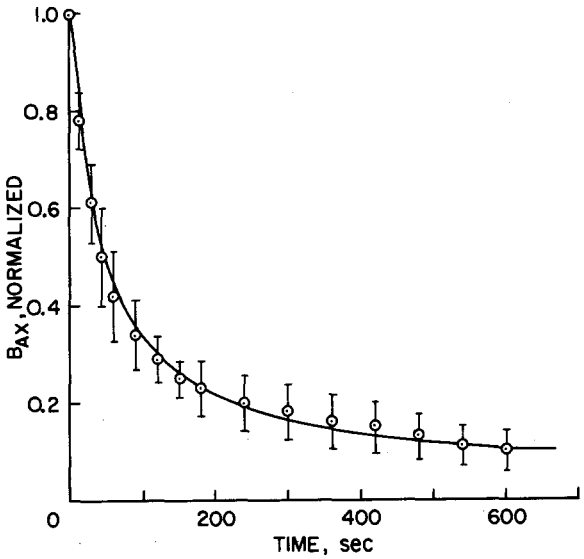

Fig. 5. Normalized transient response data, showing $f(t)$-decay characteristics of the radial component of the total surface field B_{AX} after arrival of a step transient which changes the external magnetic field radial component by an amount ΔB_{EX}, here normalized to one. The shape of the curve illustrates time characteristics of the decay of the induced poloidal eddy-current field B_P.

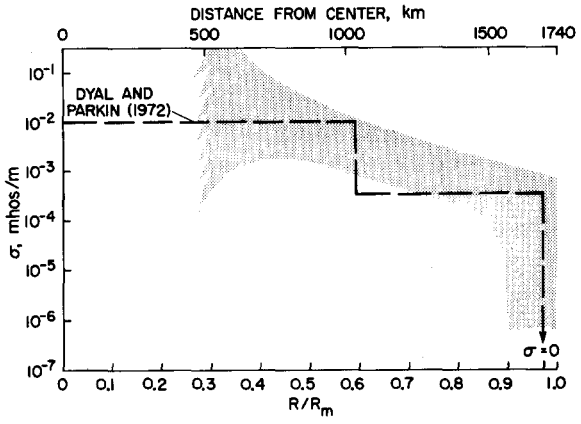

Fig. 6. Range of electrical conductivity profiles (Dyal et al., 1972b) which give radial response time-dependent curves $f(t)$ that fall within the error bars of Fig. 5. A step-function input magnetic field, modified by an initial ramp input of 15-sec rise time, is used in the analysis. The information at shallow depths is limited by the uncertainty in the rise time of the interplanetary magnetic field; that at large depths is limited by the sensitivity of the surface magnetometer. The superimposed dashed line shows the results of a three-layer Moon approximation.

Although the driving field is still approximated by a spatially uniform field, this procedure provides a better model for the very short time response.

The theoretical response curves corresponding to a large number of lunar conductivity profiles have been compared with the data of Fig. 5. It is found that a range of monotonic conductivity profiles, defining the shaded region in Fig. 6, provides fits to the data curve that fall within the error bars. The early response ($t < 20$ sec) is dominated by the finite rise time of the driving function, and hence detailed information on the conductivity at shallow depths is limited. On the other hand, a perfectly conducting lunar core with a radius of about 300 km would be undectectable for inputs less than 40 γ, so there is an inherent limitation on the conductivity information to be gained at large depths. If the conductivity function is monotonic, however, the data allow only a restricted range of conductivities at intermediate depths. The curvature of the response curve is greatest for times around 100 sec after the step input. The curvature of the theoretical curve at these times is sensitive to the conductivity at depths of 300–700 km. Hence the shape of the data curve puts fairly restrictive limits on the conductivity in this region. Deeper than 170 km, the conductivity is seen to rise from about $10^{-3.5}$ mho/m to 10^{-2} mho/m at $R/R_m = 0.45$. This is in general agreement with the three-layer model of Dyal and Parkin (1972). However, we note that conductivities greater than $10^{-1.5}$ mho/m for $R/R_m < 0.4$ are compatible with the transient data. The conductivity in the outermost layers of the Moon must be very low, less than 10^{-9} mho/m (Dyal and Parkin, 1972).

In order to define further the conductivity of the Moon, the error bars in Fig. 5 must be reduced by the analysis of more data and the theoretical treatment of more sophisticated models. Probably the most serious approximations are the neglect of the asymmetries associated with the passage of the interplanetary field discontinuity, and those associated with the boundary currents of the lunar cavity. The former affects only the very short time response, and can be studied by examining events when the solar wind speed is high. The main effect of the boundary currents is to confine the induced field to a region roughly defined by the interior of the Moon and its wake. To the order of ap-

proximation used so far, this would change the normalization of the response curve (Fig.5), but not its shape, and hence it does not change $\sigma(r)$. The effects of the confinement of the induced poloidal field to the cavity region bounded by the solar wind have been modeled by a superconducting laboratory experiment which will be discussed in section 3.1.

2.1.4. Internal lunar temperature calculations

Once a planetary electrical conductivity profile has been determined, an internal temperature distribution can be inferred if the material composition is known (see Rikitake, 1966). For cases where electrical conductivity is independent of pressure to a first approximation, the conductivity of minerals can be expressed in terms of temperature T as follows:

$$\sigma = \sum_i a_i \exp(-E_i/kT) \tag{18}$$

where E_i are the activation energies of impurity, intrinsic, and ionic modes, expressed in electron volts; a_i are material-dependent constants; and k is Boltzmann's constant. It should be emphasized that the electrical conductivity $\sigma(a, E, T)$ is a strong function of the material composition; therefore, uncertainties in knowledge of the exact composition of the sphere limits the accuracy of the internal-temperature calculation.

We calculate lunar temperature profiles (Fig.7) from the conductivity profile in Fig.6, using the expression for the electrical conductivity as a function of temperature given by England et al. (1968) for olivine and peridotite:

$$\sigma_{\text{olivine}} = 55 \exp(-0.92/kT) + 4 \cdot 10^7 \exp(-2.7/kT) \tag{19}$$

$$\sigma_{\text{peridotite}} = 3.8 \exp(-0.81/kT) + 10^7 \exp(-2.3/kT) \quad \text{in mho/m} \tag{20}$$

(In the above expressions, kT is in eV.) These conductivities are assumed to be independent of pressure below 50 kbar (England et al., 1968) and independent of frequency below 10 Hz (Keller and Frischknecht, 1966). For the example of a peridotite Moon, a temperature profile that rises sharply to 850–1050° K at $R/R_m \simeq 0.95$ and then gradually to 1200–1500°K at $R/R_m = 0.4$ is suggested by the data. At depths greater than $R/R_m = 0.4$ the temperature could be higher than 1500°K.

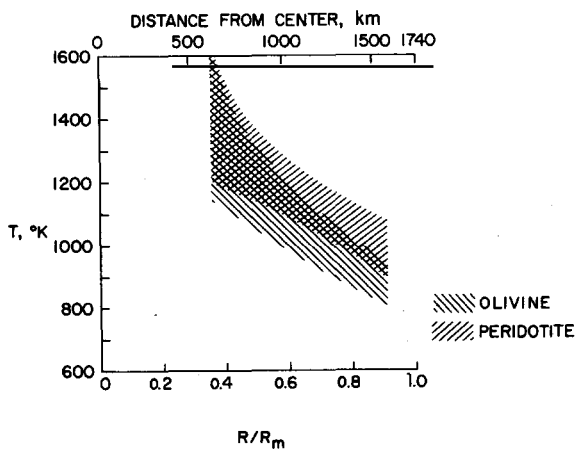

Fig.7. Temperature estimates for assumed lunar compositions of pure peridotite and olivine, calculated from the electrical conductivity profile of Fig.6.

2.2. Fourier harmonic-analysis technique

The harmonic method, as applied to the Moon, is based on the assumption that any global induced field is excluded from the oncoming solar wind by currents induced in the highly conducting solar plasma; it is assumed that in effect the solar wind completely confines the induced field in the lunar interior and in a thin region above the lunar surface. By assuming this sheath region is very thin, the confinement current is considered to be a surface current for theoretical treatment; this provides a boundary condition of total confinement by a spherical current around the whole Moon, permitting solution of Maxwell's equations below and on the lunar surface. This spherical confinement case is then applied to magnetometer data measured on the lunar sunlit side. (Basic theoretical development of harmonic solutions can be found in several references including Schubert and Schwartz, 1969; Sill and Blank, 1970.)

The harmonic analytical technique requires calculating frequency-dependent "transfer functions" which are defined as follows:

$$A_i(f) = \frac{b_{Ei}(f) + b_{Pi}(f) + b_{Ti}(f)}{b_{Ei}(f)} \tag{21}$$

$i = x, y, z$, where A_i are transfer functions of components of frequency-dependent magnetic fields, expressed in the orthogonal coordinate system with origin on the surface of the sphere ($\hat{x}$ is radial and $\hat{y}$ and $\hat{z}$ are tangent to the surface); $b_{Ei}(f)$ is the Fourier transform of the external driving magnetic field; $b_{Pi}(f)$ and $b_{Ti}(f)$ are Fourier transforms of the induced global poloidal and toroidal magnetic fields, respectively.

The harmonic data analysis approach involves Fourier-analyzing simultaneous data from the Apollo 12 lunar surface magnetometer, taken during lunar daytime, and the lunar orbiting Explorer 35 magnetometer. Then ratios of the surface data to orbital data are used to calculate a transfer function of the form of eq. 21. It is assumed that the toroidal induction mode is neglected such that the Fourier-transformed surface magnetometer data represent the sum $b_{Ei}(f) + b_{Pi}(f)$, while the transformed orbiting magnetometer data represent the driving field $b_{Ei}(f)$ alone.

The form of the transfer function is determined by the internal conductivity distribution in the Moon; therefore, a "best fit" conductivity profile can be obtained by numerically fitting to the transfer function. Fig. 8 shows the "best fit" radial conductivity profile of Sonett et al. (1971) obtained in this manner. The conductivity profile is characterized by a large "spike" of maximum conductivity about 1500 km from the lunar center. Other conductivity profiles have been calculated using the Sonett et al. (1971) transfer function, showing that the spike profile is not unique but that the frontside transfer function can be fitted by simpler two- and three-layer models (Kuckes, 1971; Sill, 1972; Reisz et al., 1972).

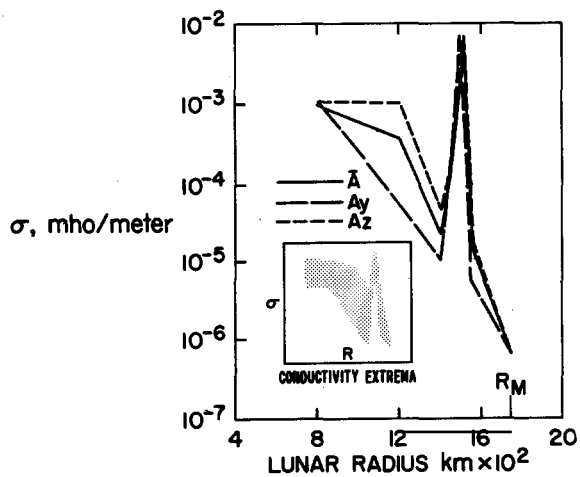

Fig. 8. Electrical conductivity profiles from Fourier harmonic analysis of lunar daytime data (from Sonett et al., 1971).

2.3. *Comparison of transient and harmonic-analysis techniques*

Since transient and harmonic techniques yield different conductivity profiles (compare Fig. 6 and 8) using data from the same magnetometers, it is useful to discuss the assumptions involved in both analyses. First we consider two basic assumptions of the harmonic technique: (a) only the poloidal induction and external driving fields are measured on the daytime lunar side; and (b) the induced poloidal field is perfectly confined by a spherically symmetric current layer. The first assumption considers that the total field measured by the lunar surface magnetometer is composed of only the external solar wind driving field $\boldsymbol{B}_E$ and the poloidal lunar response field $\boldsymbol{B}_P$. By reference to eq. 1, we recognize that various other fields may be contributing to the surface magnetometer data, e.g., interaction fields ($\boldsymbol{B}_F$) due to such effects as compression of lunar remanent fields by the solar wind plasma and generation of plasma wave modes on the sunlit side. Referring to Fig. 8, we note an asymmetry effect which is not predicted by simple harmonic-analysis theory: the harmonic analysis yields two different conductivity profiles, one calculated from y-axis (east–west) data alone and the other from z-axis (north–south) data alone. This $y-z$ asymmetry can be explained as being in part due to the daytime compression of the local remanent field at the Apollo 12 magnetometer surface site by the solar wind (Dyal et al., 1972a). Thus, when lunar daytime magnetometer data are used to study global lunar properties, knowledge of simultaneous solar wind properties is important.

The second assumption considers that the induced poloidal field is confined in the lunar sphere by the solar wind plasma. Experimentally the solar wind plasma spectrometer (Snyder et al., 1970) does not measure a confining plasma on the dark side lunar hemisphere, and the transient magnetic field data show to first order a vacuum poloidal response on the lunar dark side (Dyal and Parkin, 1971). It is questionable whether confine-

ment is complete even on the sunlit side: a subsatellite magnetometer has measured evidence of induced lunar fields at distances greater than 100 km above the lunar sunlit surface (Coleman et al., 1972), indicating that confinement is not complete over distances greater than a proton gyroradius (~ 100 km). For these reasons, the spherically symmetric plasma confinement assumption should be modified.

In summary, it is seen that magnetic fields measured on the lunar day side quite possibly involve a very complicated set of magnetic phenomena which can contribute varying magnetic field amplitudes at varying frequencies over the entire measured spectrum, and that these contributions cannot be adequately treated using the above-mentioned assumptions (a) and (b). A recent harmonic paper (Sonett et al., 1972) has considered effects such as that due to remanent field compression and response variations as a function of solar wind $\boldsymbol{k}$-vector direction with respect to the Moon. As a result, the conductivity "spike", which was emphasized earlier, is now recognized as only one of a larger set of possible conductivity profiles, some of which are much more in agreement with the transient-response three-layer models published earlier (Dyal and Parkin, 1971, 1972). Furthermore, the recent harmonic papers state that resolution of data restricts conductivity models to three or four layers rather than the eight layers used for the "spike" model.

Though of an apparently less complicated nature, there are also problems associated with the assumptions of the darkside transient analysis technique. The main problems involve: (a) the finite time required for a "step" transient to cross the lunar sphere; (b) the field increase along the antisolar line due to diamagnetic currents at the solar wind cavity boundary; and (c) deviations from sphere-in-a-vacuum theory due to partial confinement of induced fields by the solar wind. These problems are considered in section 2.1.3; the partial-confinement problem (c) is considered in more detail in the following section.

3. Interaction of the solar wind with lunar induced and remanent fields

The solar wind plasma transports the inducing magnetic field past the Moon and also interacts with the resulting poloidal-induction field and any permanent fields originating in the lunar crust. Both of these interactions have been measured by Apollo magnetometers and solar wind spectrometers.

3.1. Confinement of induced poloidal fields by the solar wind plasma

Fig. 3 schematically portrays the effects of the highly conducting solar wind on the lunar induced poloidal field; in this case the induced field geometrical configuration is altered such that the poloidal field is compressed onto the lunar surface on the sunlit side and is extended back into the cylindrical "cavity" region on the dark side. This compression has been experimentally confirmed by measurements from magnetometers on the lunar surface. For the uncompressed (vacuum) case the ratio of tangential components of surface total field ($B_{Ay,z}$) to external driving field ($B_{Ey,z}$) will have a maximum value of 1.5 (see eq. 8). Daytime ratios, however, are considerably higher than 1.5; for example, at 0.01 Hz the z-component amplication has been measured to be 3.7 (Dyal et al., 1970). Nighttime data show a smaller compressive effect in the tangential components; examples in Fig. 4B show a y-axis ratio of 2.0 and a z-axis ratio of 1.75.

The confinement of the induced poloidal field by the highly conducting solar wind is theoretically studied by considering a point dipole field inside a superconducting cylinder. Two geometrical orientations of the point dipole are considered: along the cylinder axis and transverse to the cylinder axis. (See inserts in Fig. 9 for an illustration of these orientations.) The field of the dipole oriented transverse to the cylinder axis has been determined by Parker (1962). For a dipole on the axis of a capped superconducting cylinder (of radius R), lying a distance R from the cap, the scalar potential of the confined dipole is:

$$\psi_{tc} = \frac{-2m\cos\Phi}{R^2} \sum_{n=1}^{\infty} \frac{N_n^2 J_1(N_n x/R) f_n(r)}{(N_n^2-1)J_1^2(N_n)} \qquad (22)$$

where:

$$f_n(r) = \exp(-N_n|r|/R) + \exp(-N_n(r+2R)/R) \qquad (23)$$

and Φ is the azimuthal angle measured around the axis of the cylinder, from the dipole axis; m is the dipole moment; r is the distance along the cylinder axis; N_n is the n-th root of $J_1'(N_n) = 0$.

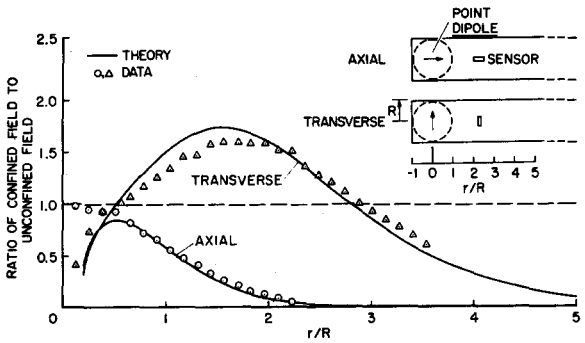

Fig. 9. Confinement of a point dipole magnetic field, shown theoretically and experimentally. The inserts schematically show lunar confinement by the solar wind, approximated by a capped-cylinder superconductor enclosing a point dipole field. The theoretical curves show ratios of confined to unconfined dipolar field versus distance along the cylinder axis. Data are results of a laboratory experiment in which confinement of a small dipole magnet's field by a cylindrical superconductor is measured experimentally.

The scalar potential which describes the field due to an unconfined point dipole is:

$$\psi_u = \frac{mx}{r^3} \tag{24}$$

The transverse component of magnetic field due to either of the potentials (eq. 22 or 23) can be calculated as a function of distance r along the cylinder axis, using $B_x(r) = -\partial\psi/\partial x$. The ratio of the transverse component of confined field to unconfined field on the cylinder axis is then:

$$\left(\frac{B_c}{B_u}\right)_{\text{trans.}} = \frac{2}{R^3} \sum_{n=1}^{\infty} \frac{r^3 N_n^3 J_1'(0) f_n(r)}{(N_n^2 - 1) J_1^2(N_n)} \tag{25}$$

where $f_n(r)$ is expressed in eq. 23; $J_1'(0) = 0.5$. This transverse confined-to-unconfined field ratio is plotted in Fig. 9.

Now we consider the effect of confinement field due to a dipole lying on the cavity axis and directed along the cavity axis (see Fig. 9, insert). The potential of the confined dipole (P. Cassen, personal communication, 1972) is:

$$\psi_{ac} = \frac{m}{2\pi} \sum_{n=1}^{\infty} \frac{J_0(k_n x)\, g_n(r)}{J_0^2(k_n)} \tag{26}$$

where:

$$g_n(r) = \exp(-k_n |r|/R) - \exp\left[-k_n\left(\frac{r}{R} + 2\right)\right] \tag{27}$$

and k_n are roots of the zero-order Bessel function. The axial components of the confined and unconfined fields are respectively $-\partial\psi_{ac}/\partial r$ and $-\partial\psi_u/\partial r$; the ratio of the radial component of confined field to unconfined field along the cylinder axis is:

$$\left(\frac{B_c}{B_u}\right)_{\text{ax.}} = \frac{1}{R^3} \sum_{n=1}^{\infty} \frac{r^3 k_n g_n(r)}{J_0^2(k_n)} \tag{28}$$

This axial confined-to-unconfined field ratio is also plotted in Fig. 9.

A laboratory experiment has been devised to examine the "axial" and "transverse" solutions (eq. 25 and 28). The highly conducting solar wind plasma cavity is modeled by a thin lead superconducting capped cylinder and the instantaneous induced poloidal field is modeled by a small dipolar samarium-cobalt magnet placed equidistant from the closed end and the side walls of the cylinder. The measured ratios of confined fields to unconfined fields are shown in Fig. 9 along with the theoretical value expressed in eq. 25 and 28.

The theory and laboratory data presented in Fig. 9 represent to first order the effects of solar wind compression on a poloidal induced lunar field, as measured by a lunar surface magnetometer positioned at the antisolar point. This compressive phenomenon, which has a measurable geometrical effect on the poloidal field, does not significantly change the time dependence of the poloidal eddy-current field. Therefore, the computed internal electrical-conductivity profile $\sigma(r)$, which is a function only of the poloidal time-dependence, will not be modified by solar wind compression to the order of approximation used here.

3.2. Compression of the permanent lunar fields by the solar wind plasma

Remanent magnetic fields have been measured by Apollo magnetometers emplaced at nine sites on the Moon. Magnitudes and locations of these steady fields are listed in Table I.

Simultaneous solar wind plasma properties have been measured at the Apollo 12 and 15 landing sites. To first order, a compression of the Apollo 12 rema-

TABLE I
Lunar surface remanent magnetic fields

Site	Coordinates	Measured magnetic fields (γ)
Apollo 12	3.2°S 23.4°W	38γ
Apollo 14	3.7°S 17.5°W	103γ and 43γ (separated by 1.1 km)
Apollo 15	26.1°N 3.7°E	3γ
Apollo 16	8.9°S 15.5°E	112γ, 113γ, 189γ, 232γ, and 327γ (separated by 0.5 – 7.1 km)

nent field in direct proportion to the solar wind pressure has been measured. For one-hour averages of measurements, the increase in magnetic field pressure $\Delta B^2/8\pi$, where $\Delta \boldsymbol{B} = \boldsymbol{B}_A - (\boldsymbol{B}_E + \boldsymbol{B}_S)$, is directly correlated to the plasma pressure nmV^2 as shown in Fig. 10. The magnetic field increases from 38 to 54 γ for a solar wind pressure increase of $7 \cdot 10^{-8}$ dyn/cm^2. The ratio of plasma pressure to *total* magnetic pressure is $\beta = 8\pi\, nmV^2/B_{ST}^2 = 5.9$, where $\boldsymbol{B}_{ST} = \boldsymbol{B}_S + \Delta \boldsymbol{B}$, during maximum plasma pressure, indicating that the stagnation condition ($\beta \leqslant 1$) is not reached and a local shock is probably not formed at the Apollo 12 site. Modulation of the remanent magnetic field by time variations in the solar wind pressure should add noise to induction measurements made on the daytime side of the Moon (Dyal et al., 1972a), as was discussed in section 2.3.

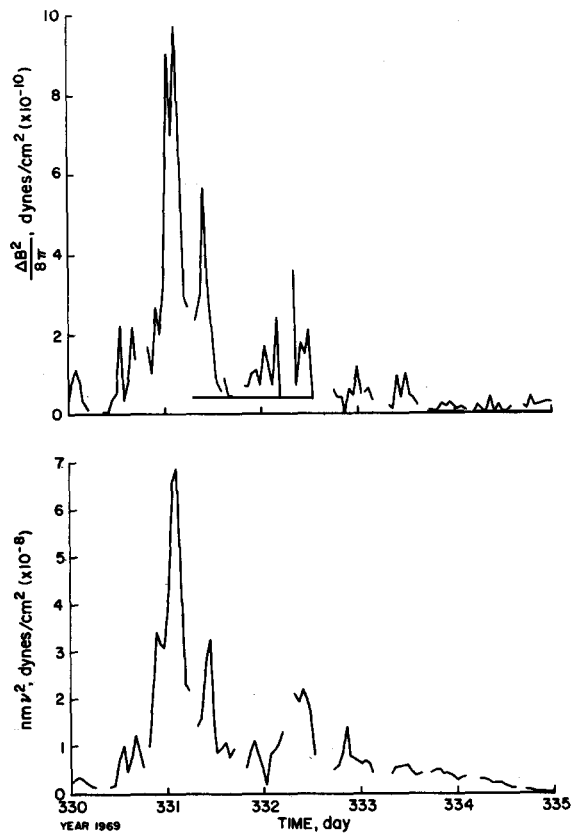

Fig. 10. Simultaneous plots of the magnetic field pressure difference $\Delta B^2/8\pi$ and solar wind dynamic pressure at the Apollo 12 surface site, showing a correlation between the pressures.

4. Magnetization field induction and permeability calculations

Referring again to eq. 1, we consider the magnetization mode $\boldsymbol{B}_\mu$. For times when all other induction and interaction modes can be neglected (e.g., for the Moon immersed in the steady geomagnetic tail field), eq. 1 can be written $\boldsymbol{B}_A = \boldsymbol{B}_E + \boldsymbol{B}_\mu$. For a sphere of permeability μ, immersed in a static magnetic field $\boldsymbol{B}_E$, the surface components of total magnetic field are expressed (Jackson, 1962; Dyal and Parkin, 1972) as:

$$B_{Ax} = (1+2F)\, B_{Ex} \tag{29}$$

$$B_{Ay,z} = (1-F)\, B_{Ey,z} \tag{30}$$

where:

$$F = \frac{(2k_m+1)(k_m-1)\left[1-\left(\frac{R_c}{R}\right)^3\right]}{(2k_m+1)(k_m+2)-2\left(\frac{R_c}{R}\right)^3 (k_m-1)^2} \tag{31}$$

Here k_m is the relative permeability μ/μ_0, R is the radius of the sphere, and R_c is the radius below which the planetary temperature is above the Curie point.

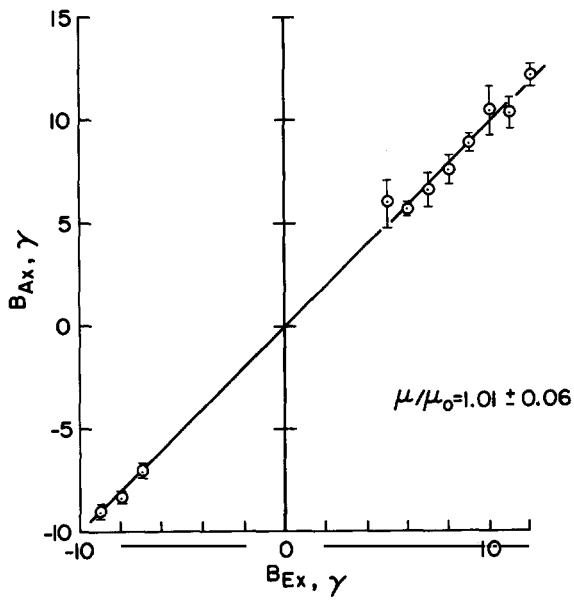

Fig. 11. Hysteresis curve of the Moon. The Moon is immersed in the steady external magnetizing geomagnetic tail field B_E (measured by Explorer 35); the total magnetic induction is $B_A = B_E + B_\mu$ measured by the Apollo 12 lunar surface magnetometer, where B_μ is the induced lunar magnetization field (the local remanent field B_S at the Apollo 12 site has been subtracted from the Apollo 12 data). In this graph only the radial (x) components are plotted. This curve is analogous to the hysteresis $B-H$ curve, where $H \equiv B_{Ex}$ and $B \equiv B_{Ex} + B_{\mu x}$. In this low-applied-field regime ($\sim 10\gamma$) the hysteresis curve is approximately linear; the slope of the curve can be used to calculate the lunar relative permeability for an assumed permeable shell thickness $\Delta R = R_m - R_c$ by using eq. 29 and 31.

A plot of B_{Ax} vs B_{Ex} is in effect a plot of a $B-H$ hysteresis curve. For cases where the ratio B_{Ax}/B_{Ex} is a constant, i.e., for low-field B_{Ex} (the average solar field is approximately 5 γ, and the geomagnetic tail field is approximately 9 γ), the hysteresis curve should take the form of a straight line. Fig. 11 shows a plot of radial components of Apollo 12 surface field (B_{Ax}) versus the geomagnetic tail field (B_{Ex}) measured by Explorer 35. A least-squares fit and slope calculations determine the factor $F = 0.0030$, which is used in eq. 31 to determine the relative magnetic permeability for a shell of inner radius R_c. For the bulk permeability of the Moon (the case $R_c = 0$), $\mu/\mu_0 = 1.01 \pm 0.06$. For a thinner permeable shell inside the Moon the permeability is higher, as shown in eq. 31.

A more accurate calculation of lunar permeability will be determined in the future from network measurements obtained at three locations on the lunar surface. The increased accuracy will make possible a calculation of the percentage of permeable iron in the outer layer of the lunar sphere.

5. Planets and satellites

To consider global electromagnetic induction in the planets and satellites, we have divided them into three main groups: (1) bodies which possess intrinsic magnetic fields strong enough to stand off the solar wind; (2) bodies with weak magnetic fields but which have an ionosphere; and (3) bodies that possess neither strong permanent magnetic fields nor ionospheres. Table II divides the planets and satellites into these three main groups based upon the limited number of measurements that have been reported.

The global inductive response to the solar wind driving field will most probably be a poloidal response for planetary bodies with either an atmosphere or a low-conducting outer crust, either of which will prevent the flow of unipolar currents and quench the toroidal mode. The probable time constant for the poloidal response is listed for each body; estimates are calculated from the Cowling time-constant expression $\tau = \mu\sigma R^2/\pi^2$, where μ is the global magnetic permeability, σ is the electrical conductivity, and R is the radius of the body. The permeability is assumed to be that of free space and conductivity estimates are based on extrapolations from lunar and Earth measurements.

The properties of planetary interiors can be studied by induction only if driving fields exist in the planetary environment which are of magnitude and frequency high enough to cause the body to respond electromagnetically. Sources of driving magnetic fields may be external to the body (e.g., solar wind magnetic field variations as shown in Fig. 1 and ionospheric diurnal variations) or internal to the body (e.g., secular variations in the intrinsic permanent magnetic fields of Earth and Jupiter). The amplitude of the solar wind field fluctuations (at a frequency of 1 Hz) vary with distance from the Sun from approximately 10 γ at Mercury's orbit, to 5 γ at the Earth, to approximately 0.8 γ at Jupiter (Scarf, 1970). The interplanetary field frequency spectrum varies as $f^{-1.5}$ (Coleman, 1968) in the solar wind near the orbits of Earth and Mars. Another driving magnetic field is that produced in the

TABLE II
Inductive response times of planets and satellites

Group	Planet or satellite	Mean radius[1] (km)	Mean density[2] (g/cm^3)	Ionosphere (+ yes; – no)	Period of primary driving field	Planetary response time constant
1	Earth	6,378	5.5	+	hours to years	1 day to 10 yr[3]
	Jupiter	70,850	1.33	+	10 h	
2	Venus	6,110	5.1	+		10 yr
	Mars	3,402	4.0	+	24 h	1 yr
	Saturn	60,000	0.7	+	10 h	
	Uranus	25,400	1.7	+	11 h	
	Neptune	24,300	1.6	+	16 h	
	Pluto	2,250	5.9	+	6 days	minutes
	Titan	2,425	2.4	+		minutes
3	Mecury	2,430	5.4	–	10 sec	days
	Ganymede	2,775	2.4	–	10 sec	minutes
	Callisto	2,500	2.1	–	10 sec	minutes
	Triton	1,885	5.0	–	10 sec	minutes
	Io	1,750	4.0	–	10 sec	minutes
	Moon	1,737	3.3	–	10 sec	2 min[4]
	Europa	1,550	3.8	–	10 sec	minutes
	Rhea	650	2.0	–	1 sec	seconds
	Tethys	600	1.2	–	1 sec	< 1 sec
	Iapetus	575	1.9	–	1 sec	< 1 sec
	Titania	455	3.4	–	1 sec	< 1 sec
	Oberon	417	8.6	–	1 sec	< 1 sec
	Dione	410	2.8	–	1 sec	< 1 sec
	Ceres	384	5.0	–	1 sec	< 1 sec

[1] Dollfus (1970); [2] Smoluchowski (1972); [3] Measured: Rikitake (1966); [4] Measured: Dyal and Parkin (1971).

ionosphere by solar radiation. In this case the magnetic field fluctuations at the planetary surface may be dominated by diurnal variations of ionospheric currents. Internal variations of the intrinsic field in a planet may produce very long period field fluctuations (e.g., the approximately 50-year secular variations in the Earth's field which are used to calculate electrical conductivity of the mantle and crust).

The induction processes in a planet will also be strongly influenced by the presence of a strong global permanent magnetic field (Spreiter and Alksne, 1970). To date, only the planets Earth and Jupiter are known to possess an intrinsic magnetic field large enough to stand off the solar wind. Venera 4 magnetometer measurements (Dolginov et al., 1969) set an upper limit for the dipole moment of Venus at $8 \cdot 10^{21}$ G. cm^3 (or $\sim 10^{-4}$ that of Earth); the Mariner 4 magnetic field measurements (Smith, 1967) set the upper limit for Mars at $2.4 \cdot 10^{22}$ G.cm^3 ($\sim 10^{-3}$ that of Earth). More recent measurements by the U.S.S.R. Mars 2 and Mars 3 magnetometers (Moscow TASS news release, 24 August 1972), however, indicate that changes in the magnetic field near Mars exceed solar wind field changes by a factor of eight and that Mars possibly possesses an intrinsic dipolar field. The Apollo subsatellite magnetomer (Coleman et al., 1972), has set an upper limit for the Moon's dipole moment of $4 \cdot 10^{19}$ G.cm^3. It is probable, however, that some of the local remanent fields on the Moon may have intensities and scale-sizes large enough to stand off the solar wind (Barnes et al., 1971; Dyal et al., 1972a).

Experimental measurements at Venus, Earth, and Mars and theoretical studies of other planets indicate that most planets except Mercury possess ionospheres with comparable peak electron densities. Ionospheres of planets listed in group 2 of Table II will damp out

TABLE II
Apollo surface magnetometer characteristics

Parameter	Apollo stationary magnetometer	Apollo portable magnetometer
Ranges (γ)	0 – ± 200	0 – ± 256
(each sensor)	0 – ± 100	
	0 – ± 50	
Resolution (γ)	0.1	1.0
Frequency response (Hz)	dc – 3	dc – 0.05
Angular response	Cosine of angle between field and sensor	Cosine of angle between field and sensor
Sensor geometry	3 orthogonal sensors at ends of 100-cm booms	3 orthogonal sensors in 6-cm cube
Analog zero determination	180° flip of sensor	180° flip of sensor
Power (W)	3.5	1.5
Weight (kg)	8.9	4.6
Size (cm)	63 X 28 X 25	56 X 15 x 14
Operating temperature (°C)	−50 – +85	0 – +50

most of the solar wind magnetic driving waves with periods less than minutes and the dominant field change occurring over the entire globe will be due to the daily formation of the ionosphere whose period will be the axial rotation period of the planet. Higher-frequency fluctuations reaching the planetary surface will be considerably lower in amplitude than the diurnal variations (on Earth the daily variations are approximately 50 γ whereas the shorter-period solar wind changes are less than 10 γ); these diurnal ionospheric magnetic field variations can induce a global response in the planet's outer layers. Since in this case the dominant driving source for the planet is geometrically in the shape of a spherical shell, many simultaneous measurements are required to describe the total inductive response and separate it into external driving and internal response fields. This formidable task has been accomplished to study the electromagnetic properties of Earth's crust and mantle (Chapman, 1919; Lahiri and Price, 1939; Ashour and Price, 1948; Rikitake, 1950, 1966; McDonald, 1957; Eckhardt et al., 1963). For the core region of the Earth, however, seismic techniques have proven to be more useful than electromagnetic induction techniques.

For the planets and satellites in group 3 of Table II which have neither a global permanent magnetic field nor an ionosphere and which do not lie within the magnetosphere of a larger body, solar wind magnetic field fluctuations should envelop the body and induce a poloidal response which can be used to study the internal properties. The bodies possessing inductive time constants comparable to driving field periods (e.g., the Moon and Io) may be better explored using electromagnetic induction techniques than by seismic methods.

Appendix: magnetic field measurement technique

Magnetic fields at the lunar surface have been measured with magnetometers emplaced by astronauts on the Apollo 12, 14, 15, and 16 missions. The three orthogonal vector components are measured as a function of time and position and telemetered to Earth. Simultaneously a magnetometer in the lunar orbiting Explorer 35 spacecraft measures the ambient solar or terrestrial driving field and transmits this information to Earth. Properties of the lunar surface magnetometers are given in Table III.

Acknowledgements

We thank Richard Hartin of Philco-Ford, Ray Stephens of the University of Santa Clara, and Jeffrey Hammill and Roy Horinouchi of DeAnza College for their valuable contributions to the laboratory superconducting experiments.

References

Ashour, A.A. and Price, A.T., 1948. *Proc R. Soc. London, Ser. A.*, 195 : 198.

Barnes, A., Cassen, P., Mihalov, J.D. and Eviatar, A., 1971. *Science*, 172 : 716.

Chapman, S., 1919. *Philos Trans. R. Soc. Lond., Ser. A.*, 218 : 1.

Colburn, D.S., Currie, R.G., Mihalov, J.D. and Sonett, C.P., 1967. *Science*, 158 : 1040.

Coleman, Jr., P.J., 1968. *Astrophys. J.*, 153 : 371.

Coleman, P.J., Schubert, G., Russell, C.T. and Sharp, L.R., 1972. In: *Apollo 15 Preliminary Science Report. NASA SP-289*, pp.22-1 – 22-9.

Debye, P., 1909. *Ann. Phys.*, 30 : 57.

Dolginov, SH. SH., Yeroshenko, Ye.G. and Davis, L., 1969. *Kosm. Issled.*, 7 vpy 5 : p. 747.

Dollfus, A., 1970. *Surfaces and Interiors of Planets and Satellites.* Academic Press, London,

Dyal, P. and Parkin, C.W., 1971. *J. Geophys. Res.*, 76 : 5947.

Dyal, P. and Parkin, C.W., 1972. *Moon*, 4 : 66.

Dyal, P., Parkin, C.W. and Sonett, C.P., 1970. In: *Apollo 12 Preliminary Science Report. NASA SP-235* : 55.

Dyal, P., Parkin, C.W., Snyder, C.W. and Clay, D.R., 1972a. *Nature*, 236 : 381.

Dyal, P., Parkin, C.W. and Cassen, P., 1972b. In: A.A. Levinson (Editor), *Proceedings of the Third Lunar Science Conference*, 3. MIT Press, Cambridge, Mass., in press.

Eckhardt, P., Larner, K. and Madden, T., 1963. *J. Geophys. Res.*, 68 : 6279.

England, A.W., Simmons, G. and Strangway, D., 1968. *J. Geophys. Res.*, 73 : 3219.

Jackson, J.D., 1962. *Classical Electrodynamics.* Wiley, New York, N.Y., p. 163.

Keller, G.V. and Frischknecht, F.C., 1966. *Electrical Methods in Geophysical Prospecting*, Pergamon, New York, N.Y.

Kuckes, A.F., 1971. *Nature*, 232 : 249.

Lahiri, B.N. and Price, A.T., 1939. *Philos. Trans. R. Soc. Lond., Ser. A.*, 237 : 509.

McDonald, K.L., 1957. *J. Geophys. Res.*, 62 : 117.

Mie, G., 1908. *Ann. Phys.*, 25 : 377.

Ness, N.F., Behannon, K.W., Scearce, C.S. and Cantarano, S.C., 1967. *J. Geophys. Res.*, 72 : 5769.

Parker, E.N., 1962. *Space Sci. Rev.*, 1 : 62.

Reisz, A.C., Paul, D.L. and Madden, T.R., 1972. *Nature*, 238 : 144.

Rikitake, T., 1950. *Bull. Earthquake Res. Inst., Tokyo Univ.*, 28 : 263.

Rikitake, T., 1966. *Electromagnetism and the Earth's Interior.* Elsevier, Amsterdam.

Scarf, F.L., 1970. *Planet. Space Sci.*, 17 : 595.

Schubert, G. and Schwartz, K., 1969. *Moon*, 1 : 106.

Sill, W.R., 1972. *Moon*, 4 : 1.

Sill, W.R. and Blank, J.L., 1970. *J. Geophys. Res.*, 75 : 201.

Smith, E.J., 1967. In: W.R. Hindmarsh, F.J. Lowes, P.H. Roberts and S.K. Runcorn (Editors), *Magnetism and the Cosmos.* Oliver and Boyd, Edinburgh.

Smoluchowski, R., 1972. In: *Physics of the Solar System. NASA SP-300* : 269.

Smythe, W.R., 1950. *Static and Dynamic Electricity.* McGraw-Hill, New York, N.Y.

Snyder, C.W., Clay, D.R. and Neugebauer, M., 1970. In: *Apollo 12 Preliminary Science Report, NASA SP-235* : 75.

Sonett, C.P., Colburn, D.S., Dyal, P., Parkin, C.W., Smith, B.F., Schubert, G. and Schwartz, K., 1971. *Nature*, 230 : 359.

Sonett, C.P., Smith, B.F., Colburn, D.S., Schubert, G. and Schwartz, K., 1972. In: A.A. Levinson (Editor), *Proceedings of the Third Lunar Science Conference, 3.* MIT Press, Cambridge, Mass.

Spreiter, J.R. and Alksne, A.Y., 1970. In: *Annual Review of Fluid Mechanics*, 2 : 313–354.